Mechanical Systems and Signal Processing 66-67 (2016) 793–810

Contents lists available at ScienceDirect

Mechanical Systems and Signal Processing

journal homepage: www.elsevier.com/locate/ymssp

OPTYRE – A new technology for tire monitoring: Evidence of contact patch phenomena

N. Roveri [a,*], G. Pepe [b], A. Carcaterra [b]

[a] CNR-INSEAN, Via di Vallerano, 139, 00128 Rome, Italy
[b] Department of Mechanics and Aeronautics, University of Rome, "La Sapienza", Via Eudossiana, 18, 00184 Rome, Italy

ARTICLE INFO

Article history:
Received 2 May 2015
Received in revised form
11 June 2015
Accepted 20 June 2015
Available online 14 July 2015

Keywords:
Smart tire
Theory of tire
Friction estimation
Active safety

ABSTRACT

The present paper contains the description of a new technology for optical strain measurements in rolling tires. The apparatus is based on the use of Fiber Bragg Gratings sensors and light spectrum analyzer. With the help of a new analytical model, describing the tire strain during its revolution, the experiments permit, for the first time, to provide evidence of the transition along the contact patch between the grip and the slip regions. Moreover, the contact patch is identified and the experimental evidence suggests that the existing methods provide underestimated lengths.

1. State of art in the field of intelligent tire

The World Business Council for Sustainable Development proposed seven goals to improve the prospects for sustainable mobility. Among those are reduced conventional emissions, reduced transport-related noise and reduced number of transport-related deaths and injuries. The challenges imposed by a more sustainable mobility are affecting the design of tires. Companies, more and more, are forced to compromise between several aspects of the tire performances that are bound together, in order to produce less noisy and less energy-consuming tires with increasing grip performances.

Research and technological advances in tire development are then focused on increasing the vehicle safety, improving vehicle stability and control, and attempting to maximize the longitudinal and lateral forces between tire and road. The emerging capability derived from the integration between mechanics, electronics and control, allowed for a radical change in the prospective of vehicle safety that nowadays relies more on active control systems. Active control systems use information about vehicle dynamics to improve the safety by detecting and minimizing skids. Existing devices, such as Traction Control, Electronic Stability Program, etc., rely on the indirect estimation of vehicle dynamics variables, such as forces, load transfer and tire–road friction, using on board sensors: the more precise and fast the estimation, the better the performances of the control system.

The development of an embedded sensor system for monitoring key variables, such as pressure, strain, temperature, acceleration, wheel loading, friction and tread wear, is a hard task and requires advanced technologies in the field of sensors and data transmission methods. Moreover, the design of data transmission and power supply systems are further challenging tasks. In fact, the sensor-tire rubber compatibility, the difficulties of embedding large-sized sensors in the

* Corresponding author.
E-mail address: nicola.roveri@gmail.com (N. Roveri).

http://dx.doi.org/10.1016/j.ymssp.2015.06.019
0888-3270/

interior space of the tire, the high static pressure and high accelerations of the environment inside the tire, which is generally harsh and hostile for the integration and reliability of sensors, the economic impact of using expensive sensors in comparatively inexpensive products are problems which need to be solved for the fruitful design of the intelligent tire.

The use of tire as a sensor has been the focus of numerous research studies and patents in the last twenty years, with special attention to friction identification [1–10]. Concerning indirect variable monitoring, the variable of interest is extrapolated from the sensed parameters, which are mainly vehicle velocity and wheel angular speed [1], for e.g. Yi et al. [2] used the wheel slip, the vehicle velocity and the normal load on the tire to determine the friction coefficient. Due to nonlinear relationships among tire parameters, quantitative relations are difficult to acquire and fuzzy logic controller [3] or Kalman filter [4] has been used. Even though indirect methods use existing sensors and are easy to install, their accuracy is low and a calibration is often required when one or more tires are substituted or when the pressure is adjusted [4].

Opposite to the indirect techniques, direct methods have higher accuracy; since the sensitivity is related to particle size, MEMS are suited for high-sensitivity pressure sensors [5]. Tjiu et al. [6] used MEMS sensors for tire condition monitoring system. Yi [7] used polyvinylidene fluoride-based sensors to measure the tread deformation. Surface acoustic wave (SAW) sensors have been investigated for monitoring the applied strain [8].

However, direct or indirect sensing methods only permit to acquire data with poor time and spatial accuracy, they are not able to sense and transmit high speed dynamic quantities [7]. More research is indeed required for better resolution. In spite of the technological advances, commercial transducers to measure directly the tire–road friction coefficient which can be adopted for applications are still not available. Recent advances in sensors and related electronics that allowed to gain accurate and real time estimation produced further solutions opening the way to potential industrial products [9] as in the case of Cyber Tyre [10].

In this context, the need of simple measurements together with the requirement of reliable identification processes makes this field challenging, where new investigations and potential solutions are needed. This paper is part of a research project [11,12] focused on the development of a new system for the real-time identification of the tire stress during rolling and residual grip estimation. In this context, three different goals and relative lines of research are in progress:

I. Development of an appropriate sensor technology by means of optical sensor measurements. The present paper is based on the results of a new patent [12] and describes the continuous tire strain acquisition by means of optical sensor measurements. The setup comprises one or more fibre optics provided with Fiber Bragg Grating sensors fixed to the, internal or external, surface of the tire, and adapted to record data regarding the deformation of the tire carcass.
II. Identification of the tire–road contact conditions, which relies on a new model of tire dynamics that takes inspiration from the Brush Road Beam model [11], with the advantage of providing information also outside the contact patch. The model aims to provide qualitative information of the tire behavior under dynamic conditions, which helps the comprehension of the experimental data and forms the basis of a technology for grip identification focused on strain rather than acceleration measurements. This approach is different from others developed in similar industrial research projects [9,10]. In fact, the most advanced technologies for grip identification are based on the use of MEMS, which measures the acceleration at some points of the tire's inner structure. The different choice of measurement strategies, acceleration versus strain, has a series of deep implications in terms of sensors, models and algorithms employed and at the end outlines two completely different technologies of grip identification.
III. Use of the grip information to control the electronic assisted drive devices, which will be the object of a future work.

The paper is organized as follows. Section 2 presents the experimental apparatus developed and adopted for the test campaign. In Section 3 the theoretical model of tire, based on infinite beam on elastic foundation approximation, is presented. Theoretical results open the way for the experimental identification of the tire footprint and of the tire–road grip conditions. They are validated in Section 4, where the signals acquired during the experimental test campaign are presented. Finally, Section 5 presents some perspectives of the work and draws some conclusions.

2. Light beam running into the tire: the OPTYRE system

The present apparatus allows the acquisition of the tire strain along an array of measurement points which consists of FBG sensors.

Bragg gratings are made by illuminating the core of the optical fibre with a spatially-varying pattern of ultra violet (UV) laser light. A periodic spatial variation in the intensity of UV light produces a corresponding periodic variation in the refractive index of the fiber. The modified optical fiber becomes a wavelength selective mirror: the light transmitted along the fiber is partially reflected at each index variations, but these reflections interfere destructively for the majority of wavelengths and the light propagates down the fiber almost uninterrupted. However, at one particular narrow range of wavelengths, constructive interference takes place and light is reflected back to the fiber.

Therefore, an FBG sensor is a distributed Bragg reflector, i.e. a periodical variation of refractive index inside the core of optical fiber, as in Fig. 1, able to reflect a particular wavelength of light and transmit all the others. The reflected Bragg wavelength λ_B is related to the refractive index of the fibre n and to the period of the refractive index modulation Λ by the formula: $\lambda_B = 2n\Lambda$. Thus the FBG is a strain sensor which measures the local axial deformation of the optical fibre.

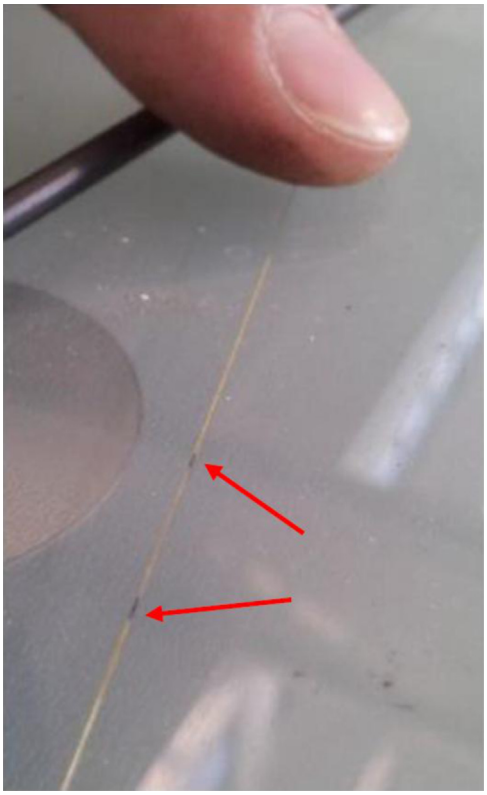

Fig. 1. Optical fiber with one FBG, the sensor lies within the black marks on the line.

The previous relationship implies that the reflected wavelength λ_B is modified by any variation in the physical or mechanical properties of the grating sensor. As an example, strain on the fibre alters Λ and *neff* through stress optic effect. Likewise, changes in temperature modify *neff* via the thermos optic effect and when the fiber is unconstrained, Λ is influenced by thermal variations. These phenomena are enlightened in Eq. (2.1), where the first term on the right hand side gives the effect of strain on λ_B and the second describes the influence of the temperature.

These perturbations can be determined by monitoring the wavelength change of the FBG sensor: the acquisition of strain in the presence of important temperature excursions requires the use of two FBG sensors in pairs, one for the strain, which is bonded to the structure of interest and one for the temperature, close to the first but isolated from strain, responding to temperature variations only.

Characteristic wavelength variations of FBG sensor, with a central wavelength of 1550 nm, due to mechanical strain and temperature change are roughly 1 pm/$\mu\varepsilon$ and 10 pm/°C. FBG sensors allow distributed sensing over significant areas by multiplexing a large number of sensors on a single fiber, which are immune to electromagnetic interference and have compact size. Due to all these advantages, they have been widely used in many applications for the structural health monitoring [16].

The core of the system is the embedding of one, or more, optical fiber equipped with several FBG sensors along the tire circumference. In particular, the internal or the external surface of the tire is equipped with one or more FBG sensors mounted along one or more optical fibers, as in Figs. 2 and 3, respectively. These FBG sensors are utilized to record the local deformation of the tire carcass, by means of measuring the frequency of the light reflected from the various sections of the fibre where an FBG sensor is present.

The advantage of pasting them into the inner surface is the fiber protection in dynamic tests, while the cons are the need for drilling the rim, as in Fig. 4. This operation is necessary to connect the optical fibre with the rotary coupler, in Fig. 5. The solution of placing the fibre inside the tire produces the risk that the fibre gets broken by the tire changer machine during mounting/dismounting operations. Mounting the fibre along the external tire circumference is an easier set-up, even if the sensors have to be protected from the direct contact with the ground, as in Fig. 3.

These solutions are suited for tire prototypes, while a practical implementation of the proposed system for industrial application is under development, which permits an easy installation/vulcanization of the optical fiber along the inner liner of the tire, protecting the sensor form the external environment.

The measurement scheme is shown in Fig. 6 whose schematic description is provided ahead:

- A light beam signal, in the range of far infrared wavelengths, is generated by an optical led source; the light beam travels

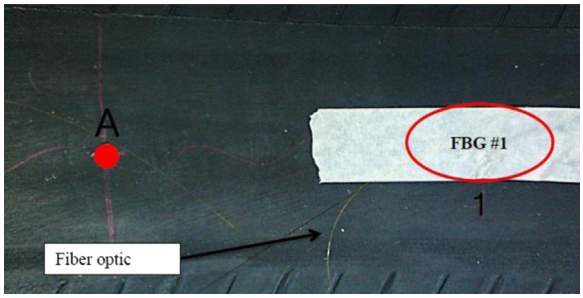

Fig. 2. Optical fiber pasted into the inner liner.

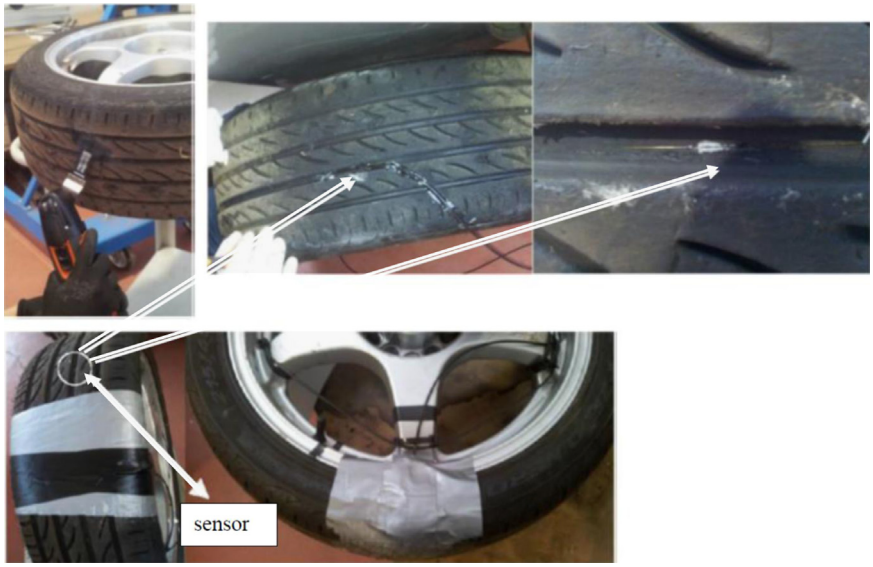

Fig. 3. Optical fiber pasted into the central groove of the tire tread. Preparation of the tire for the placement along the external circumference, the scotch tape protects the FBG sensors from the contact with the ground.

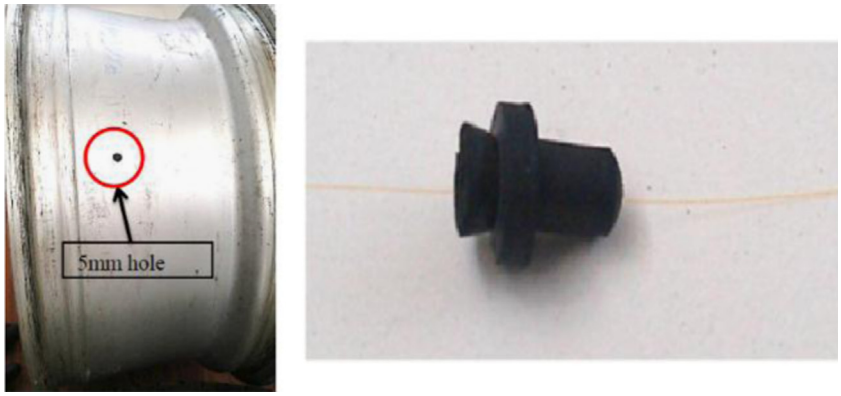

Fig. 4. The rim needs to be drilled and the hole sealed with a proper rubber-valve.

along an optical fiber equipped with FBG sensors attached to the tire circumference.

- When the tire is deformed, the frequency bandwidth of the reflected light changes and such variation is detected by a spectrum analyzer.
- The spectrum analyzer samples the analogical signal before sending it to the computer, where the signal can be suitably processed.

The FBG interrogator used here is the Smartscan by Smart Fibers [22]. The unit serves as a laser source and spectrum analyzer; it has a wavelength range of 40 nmand is equipped with four measurement channels, and the maximum number

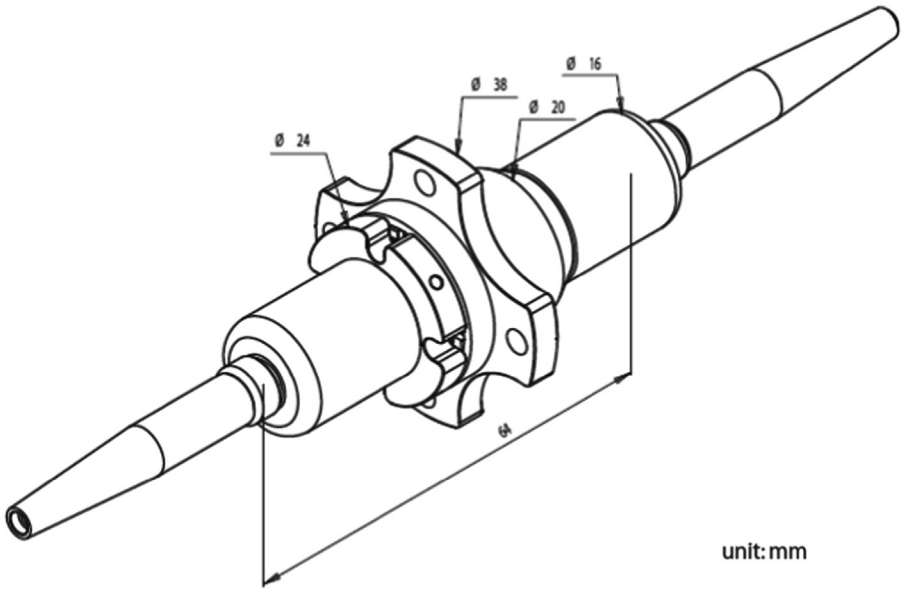

Fig. 5. Basic dimensions of the rotary coupler.

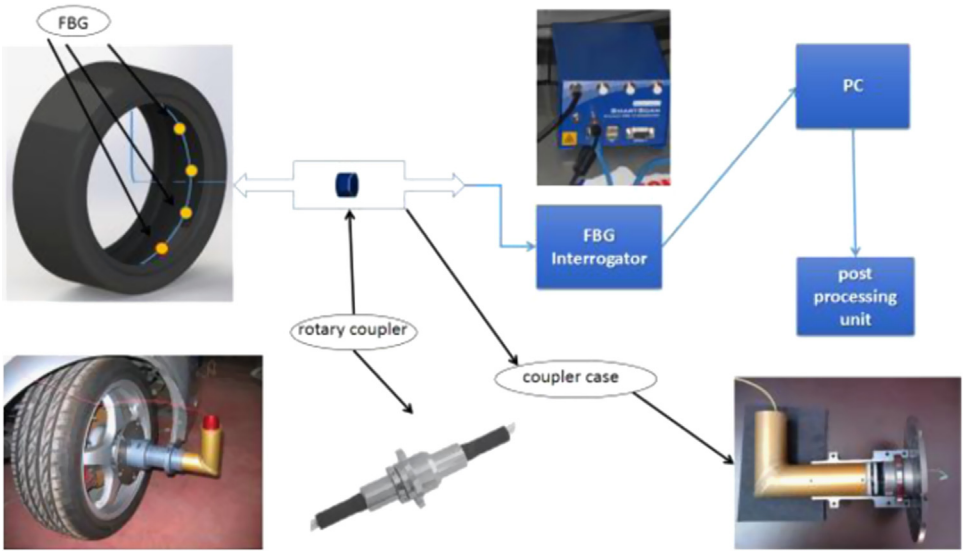

Fig. 6. Measurement scheme of the OPTYRE system.

of sensors per channel is 16, with minimum and maximum sampling rate of 2.5 and 25 kHz per sensor per channel, respectively. A detailed description of the specification can be found to the manufacturer's web site. The interrogator reads the instantaneous wavelength $\lambda_j(t)$ of each FBG sensor, which is related to the local strain $\varepsilon_j(t)$ by the following formula:

$$\varepsilon_j(t) = K_\varepsilon \frac{\lambda_j(t) - \lambda_{0j}}{\lambda_{0j}} - \alpha \Delta T \tag{2.1}$$

where λ_{0j} is the reference wavelength for the j-th FBG sensor, $K_\varepsilon = 1.27$ is the constant of proportionality, ΔT the temperature variation during the experiment, which is roughly zero in our tests, and α is the coefficient of thermal expansion.

The FBG interrogator is integral with the car chassis; therefore to allow the acquisition under dynamic condition, a fiber optic rotary coupler, in Fig. 5, is interposed between the tire and the interrogator. The rotary joints are the same to optical signals as the electrical slip rings are to electrical signals, a means to pass signals across rotating interfaces, allowing uninterrupted data transmission while rotating. A schematic representation of the coupler is provided in Fig. 5. The rotoric flange of the coupler has to be coaxial with the tire axes and integral with the rim, while the statoric flange has to be rigidly

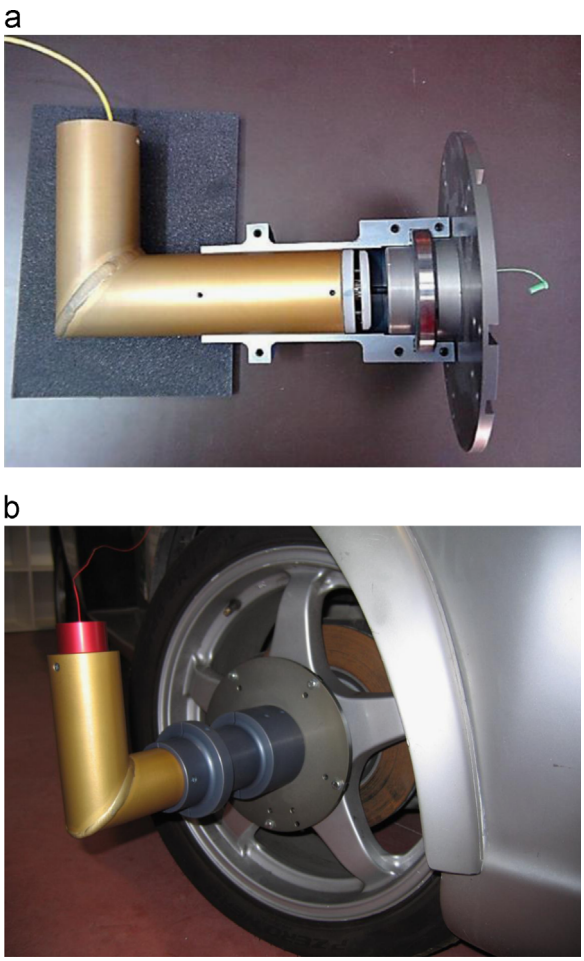

Fig. 7. Coupler case attached to the rim.

connected with the car chassis. These tasks are carried out with a properly designed coupler case, in Fig. 7, which protects the rotary joint from rubbles and allows an easy connection to the wheel.

The present setup overcomes the main difficulties of the technologies of the prior art, both relating to the power supply system and to the data transmission system. The power generator supplying the FBG sensors is integral to the affixed parts of the vehicle and external to the tire; this generator consists of one light source that transmits light to the fibre optic, which is integral to the tire carcass, by means of the contactless rotary optical coupler. The optical signal sent on-board the tire is modulated passing through the FBG sensors and reflected outside the tire by means of the rotary optical coupler itself, which thus replaces each data transmission device. One of the main advantages of this technological solution is that the same physical light beam carries both the power to sensors and the information to the interrogator.

Further advantages of the present setup arise from the material of these sensors, which have low rigidity and are capable of long-term acquisitions, even under adverse conditions encountered by the tires, and are highly compatible with the rubber of the tire.

The tire used for the present setup has the size 215/45 R17, it is installed on a prototype vehicle shown in Fig. 8.

3. Analytical model for the strain distribution over the tire surface

A propaedeutic analysis based on a simple theory of strain along a rotating tire is needed before showing the experimental results. In fact, this theoretical background helps in an easier interpretation of the experiments. This connection is frequently missed in the technical literature on experimental tire analysis. Moreover, this approach to the radial dynamic of tires has its own value since, as far as the authors know, it has never been considered before. Additionally the model allows for closed form solutions. The chance this analysis opens is to permit the understanding of the strain trend along the entire circumferences of the tire. Moreover, a sharp focus is on the identification of the position of the transition between slip and non-slip regions, and of the length and position of the tire–road contact patch.

Fig. 8. Intelligent tire mounted on the prototype vehicle.

The deformation of the contact patch of the tire, induced by static or dynamic forces, is here studied with a simplified model based on an infinite beam on elastic foundation to represent the tire. The toroidal shape of the tire is rectified, the tread is assumed to have the characteristics of an infinite beam attached to the elastic structure of the sidewalls, which is modeled with an elastic foundation of the Winkler type. We shall see, the proposed model of tire offers results qualitatively similar to those in the existing literature [11,17], with the advantage [11] of providing information outside the contact patch without the need of a complex formulation of the equations of motion [15–17].

On these assumptions, the transverse vibration w of the beam is described by the differential equation as follows:

$$EJ\frac{\partial^4 w(x,t)}{\partial x^4}+\mu\frac{\partial^2 w(x,t)}{\partial t^2}+kw(x,t)=P(x)\delta(x-ct) \tag{1}$$

where x and t are the space and time independent variables and EJ, μ, and k are the flexural stiffness, the mass per unit length and the coefficient of the Winkler foundation, respectively. P is the vertical load, moving with a constant velocity c and $\delta(x)$ is the Dirac delta function. The model and the sign convention are depicted in Fig. 9.

In case of concentrated load, the quasi-stationary solution is obtained with the following procedure. It is convenient to introduce the new independent variable:

$$s=\lambda(x-ct) \tag{2}$$

with

$$\lambda=\sqrt[4]{\frac{k}{4EJ}} \tag{3}$$

Eq. (2) is dimensionless and shows the origin of the new reference system moves together with the load at uniform speed c. For the quasi-stationary state, the solution of Eq. (1) will be in the form $w(x,t)=w_0\tilde{w}(s)$, which is the product

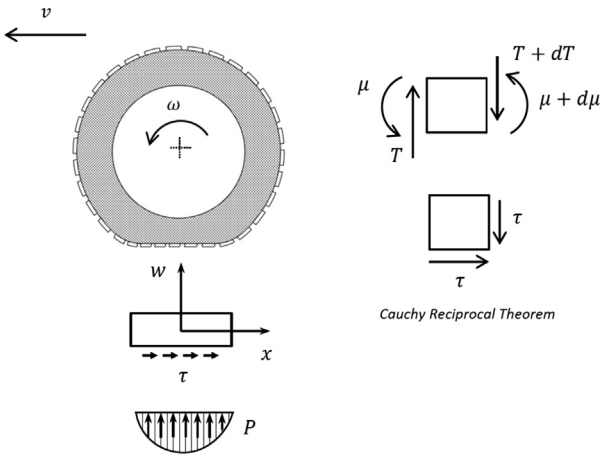

Fig. 9. Model of the tire and reference system.

between the dimensionless deflection and the static deflection of beam:

$$w_0 = \frac{P}{8\lambda^3 EJ} = \frac{P\lambda}{2k} \tag{4}$$

underneath the static load P.

Substituting Eqs. (2)–(4) into Eq. (1), after some algebra, gives the ordinary differential equation of the fourth order:

$$\frac{d^4\tilde{w}(s)}{ds^4} + 4\alpha^2\frac{d^2\tilde{w}(s)}{ds^2} + 4\tilde{w}(s) = 8\delta(s) \tag{5}$$

where the dimensionless parameter α is

$$\alpha = \frac{c}{c_{cr}} = \frac{c}{2\lambda}\sqrt{\frac{EJ}{\mu}} \tag{6}$$

with

$$c_{cr} = 2\lambda\sqrt{\frac{EJ}{\mu}} \tag{7}$$

the critical speed of the beam. Using the following boundary conditions:

$$s \to \pm\infty: \qquad \tilde{w}(s) = \tilde{w}'(s) = \tilde{w}''(s) = \tilde{w}'''(s) = 0 \tag{8}$$

The solution of Eq. (5) is found by the method of Fourier integral transformations:

$$\tilde{w}(s) = \frac{1}{ab}e^{-b|s|}(a\ \cos\ as + b\ \sin\ a|s|) \tag{9}$$

where

$$a = \sqrt{1+\alpha^2},\ b = \sqrt{1-\alpha^2} \tag{10}$$

Through the stress–strain relationship, using the sign convention in Fig. 9, the beam deformation is given by

$$\varepsilon = \frac{M}{EJ}y = w''y \tag{11}$$

where ε is the strain in the x direction at distance y from the neutral axis.

Let us now focus on the load P, which should take into the account the effect of vertical and frictional, i.e. tangential forces, which are evaluated following the well-known brush-model.

The vertical force acting on the contact patch of the tire is related to the car weight and is usually approximated with the parabolic function:

$$p_{ver}(x) = \gamma\left(L^2 - x^2\right) \tag{12}$$

where $\int_{-L}^{L} p(x)dx = M$ is the total force, which is distributed over the length $2L$ of the contact patch and $\gamma = (3M/4L^3)$. Eq. (12) does not consider rolling resistance, which affects vertical stress and creates a resisting moment against tire rolling.

Table 1
List of symbols and their values.

List of symbols	
$E=5\cdot10^{7}$ N	Tire Young modulus
$J=1.66\cdot10^{-8}$ m^4	Beam area moment of inertia
$\mu=1100$ kg/m	Tire mass per unit length
$k=7.790\cdot10^{6}$ N/m^2	Elastic constant of the Winkler foundation
$R=0.3126$ m	Unloaded radius of the tire
$h_t=0.018$ m	Tire section height
$L=0.05$ m	Semi footprint length
$M=400\cdot9.81$ N	Total load over the footprint
$C_x=1.883\cdot10^{6}$ N/m	Longitudinal slip coefficient
$f_s=0.8$	Static tire–road friction coefficient
$f_d=0.6$	Kinematic tire–road friction coefficient
$c=11.11$ m/s	Speed of the moving load

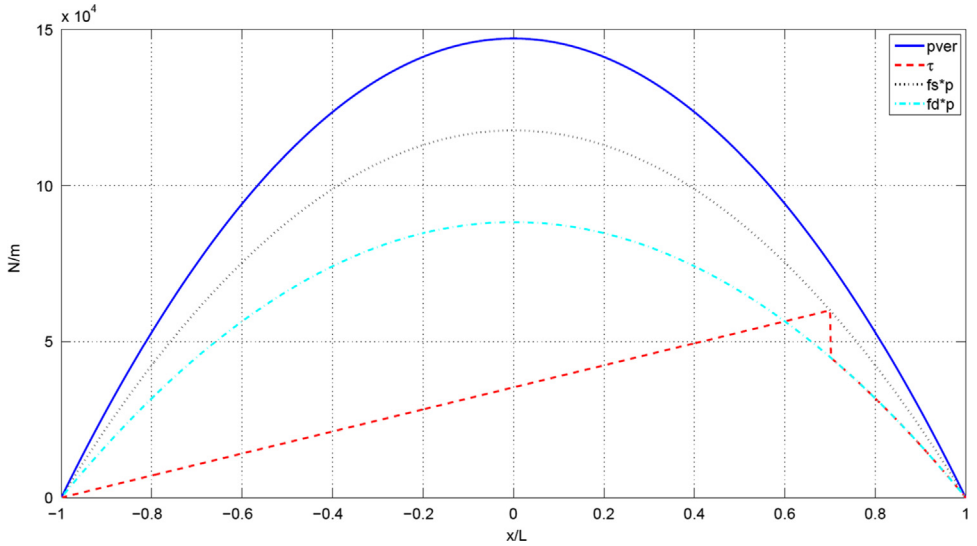

Fig. 10. Vertical and frictional forces per unit length acting on the footprint, in blue and red lines, respectively. (For interpretation of the references to color in this figure legend, the reader is referred to the web version of this article.)

The frictional force arising from the longitudinal motion of the tire is tangential to the contact patch and can be defined as follows:

$$\begin{cases} \tau(x) = \mp \sigma C_x(x+L), & |\tau(x)| \le f_s p(x) \\ \tau(x) = \mp f_d p(x), & \text{elsewhere} \end{cases} \tag{13}$$

where the signs $-$ and $+$ are for driving and braking torque applied to the tire, respectively, σ and C_x are the longitudinal slip ratio and stiffness coefficient of the tire (typical value $1.5\cdot10^{6}$ N/m), f_s and f_d are the static and dynamic friction coefficient, respectively.

The slip ratio is defined as

$$\sigma = 1 - \frac{\omega R}{V}, \quad \sigma \in [-\infty,\ 1] \tag{14}$$

where R and ω are the radius and the angular speed of the tire, respectively, while V is the forward velocity of its center. When a braking torque is applied the peripheral speed of the tire, i.e. ωR is smaller than V; thus the slipping ratio is positive; the opposite is true for a driving torque. In the present model the speed of the moving load, c in Eq. (1), is the peripheral speed of the tire, ωR.

Eq. (13) shows the frictional force per unit length is zero at the edges of the tire. When a braking torque is applied the frictional force increases linearly up to the maximum value $f_s p(x_s)$. This is the friction limit between the tire and the road and the force acting on the tread element starts to slide when the deformation reaches this value. In the sliding region, the frictional force decreases as the vertical pressure decreases, as stated by the Coulomb model.

3.1. Identification of the slip and non-slip transition

Using the first part of Eq. (13), together with Eqs. (14) and (12), the relation that links the transition abscissa x_s, for which $\tau(x_s)=f_s p(x_s)$, to the slipping ratio and to the other parameters of the model is found to be

$$|\sigma| = (L-x_s)\frac{\gamma f_s}{C_x} \tag{15}$$

Eq. (15) shows that the present model is able to fulfill the physical constraints between x_s and σ, if the stiffness coefficient is properly selected. When the slip ratio is zero the transition abscissa is located at the trailing edge, i.e. $x_s=L$, and the whole contact patch is in adhesion with the road surface. The second constraint arises for the effect of an intense torque applied to the tire; the whole contact patch may slip, thus the transition abscissa falls at the leading edge, i.e. $x=-L$, and Eq. (15) becomes

$$\left|\sigma\right| = \frac{2\gamma f_s}{C_x} \tag{16}$$

under this circumstances $|\sigma|=1$ and Eq. (16) is verified if

$$C_x = 2\gamma L f_s \tag{17}$$

It is worth pointing out that the stiffness coefficient imposed by Eq. (17), with the parameters in Table 1, is $1.88\cdot10^6$ N/m: this value is meaningful for commercial tires, whose stiffness coefficients are in the order of $(1.5\div2)\cdot10^6$ N/m.

Fig. 10 shows the vertical and frictional (braking) forces per unit length acting on the contact patch, evaluated with Eqs. (12) and (13), respectively, plotted with $\sigma=0.15$ and the other parameters listed in Table 1. The transition between the adhesion and the slipping zone is enlightened by the discontinuity on the tangential stress curve.

The contribution of the frictional force (13) to the vertical load P in the right hand side (RHS) of Eq. (1) is now evaluated, considering an infinitesimal element of the tread, with the sign convention in Fig. 9, and applying the Cauchy Reciprocal Theorem:

$$p_{fri}(x) = h\frac{d\tau(x)}{dx} \tag{18}$$

where h is the tread height.

Since solution (9) of Eq. (1) holds for a concentrated load, using the superposition principle, the RHS of Eq. (1) is approximated by

$$\sum_{i=1}^{n} \Delta x\left(p_{ver}(x_i)+p_{fri}(x_i)\right)\delta(x-x_i-ct) \tag{19}$$

where $x_i=(i-1)\Delta x-L$, with $\Delta x=2L/(n-1)$ and $i=1, 2,\ldots, n$ where n is the number of discretization points. Eq. (19) keeps into the account the global effect of the distributed vertical and frictional forces per unit length, Eqs. (12) and (18) respectively, acting on the contact patch of the tire.

Fig. 11 shows the vertical displacement of the tire (9), the longitudinal deformation (11), and its first derivative, when a braking torque is applied with $\sigma=0.15$. The infinite beam approximation is adopted and the distribute load (15) is substituted into the RHS of Eq. (1), with the parameters listed in Table 1.

a) The maximum displacement is roughly 0.8 cm; this value is in line with the maximum radial tire deflection under static load for commercial car tires.
b) Recalling that y in Eq. (11) is the distance from the neutral axis, the longitudinal strain is evaluated at $y=h_t/2$, namely along the inner surface of the tire, which is compressed in the areas where the tire contacts with the road surface, and is mainly strained over the rest of the contact patch. The frictional stress produced by the braking torque makes the strain asymmetric in respect of the centre of the footprint: the area around the trailing edge is more compressed than the one around the leading edge. From Eq. (11), it is clear the outer surface of the tire, at $y=-h_t/2$, has the same strain plot with the sign changed: the tread in contact with the road is mainly compressed over the contact patch.

The discontinuity on the spatial derivative of the strain curve, close to the trailing edge, is due to transition between the adhesions to the slipping areas, which causes the jump on the tangential stress curve, as in Fig. 10, and allows identification of the transition abscissa from experimental data.

To understand the contribution of the vertical load and of the rotational torque to the tire deformation, two different solutions are evaluated setting apart the vertical and frictional forces, Eqs. (12) and (18), into the RHS of Eq. (1); results are plotted in Fig. 12.

- Given the symmetry of the vertical load (12), the corresponding tire deformation and strain plots are also symmetrical.
- When the braking torque is applied, shear deformations due to the frictional load (18) arise and give rise to an asymmetrical strain distribution, as stated by Eqs. (13) and (18). This point offers a different perspective in respect to the

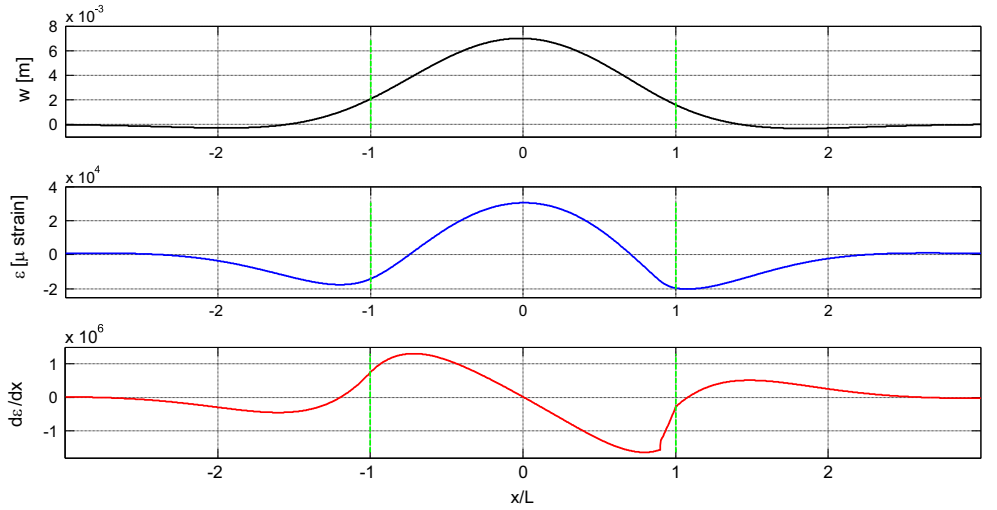

Fig. 11. Starting from the subplot on top, the vertical displacement, the longitudinal deformation, and its derivative, of the infinite beam subjected to the distributed moving load (15). The vertical dashed lines are in correspondence of the footprint limits: the leading and trailing edges are on the negative and positive part of the *x*-axis, respectively. The extrema of the first derivative of the strain fall well within the contact patch.

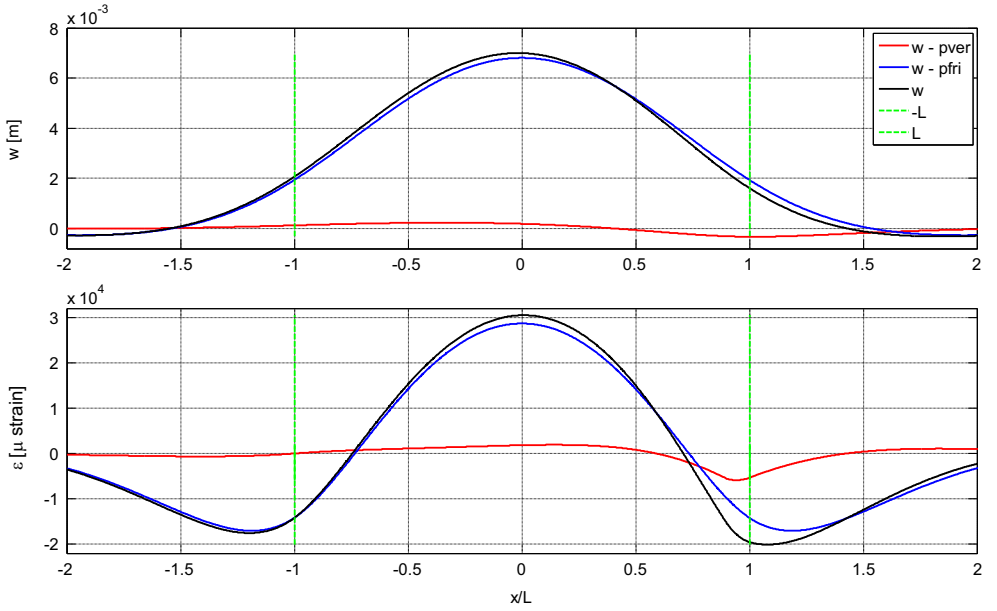

Fig. 12. Vertical displacement and strain components considering the isolated effect of the vertical and frictional loads, respectively Eqs. (12) and (14), plotted in blue and red lines. Black lines are the total displacement and strain plotted for reference. (For interpretation of the references to color in this figure legend, the reader is referred to the web version of this article.)

existing literature [13], which predicts the strain induced by the frictional load is antisymmetric in respect to the centre of the footprint.

The effect of the braking torque strength on the tire deformation is studied selecting different values for the slip ratio in the previous equations: results are displayed in Fig. 13. As the slip ratio increases the maximum strain point moves from the centre toward the leading edge of the contact patch.

With the aid of Fig. 13, for small slip ratios, i.e. $\sigma < 0.15$, the transition abscissa falls in the neighborhood of the trailing edge, as stated by Eq. (15), and the slope change along the strain curve is barely perceptible. In these cases, the experimental identification of the transition abscissa is more problematic, since ambient and numerical noise together with inadequate time sampling may hide the discontinuity on the first derivative of the strain curve. It should also be noticed, for small slip

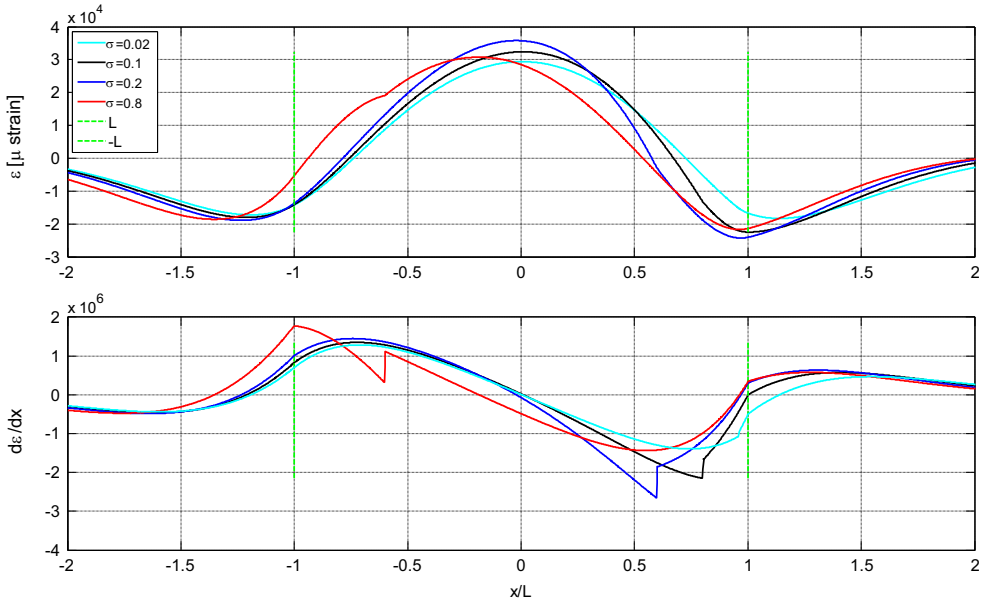

Fig. 13. The longitudinal deformation, and its derivative, plotted for four different slip ratios.

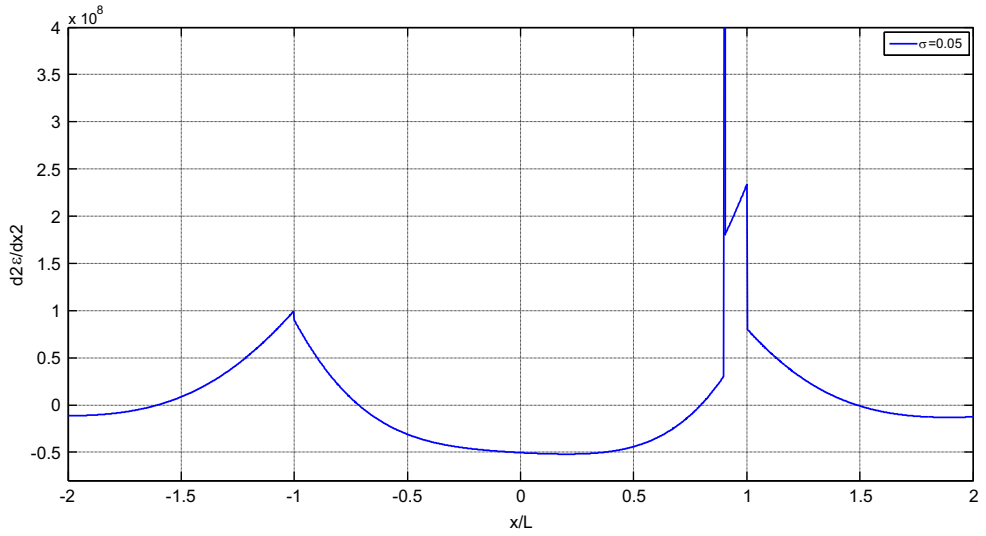

Fig. 14. Second derivative of the tire strain, plotted versus the normalized abscissa.

ratios, the first spatial derivative of tire strain is roughly symmetric in respect to the centre of the footprint, as in Figs. 11 and 13.

3.2. *Identification of the contact patch*

Concerning the experimental identification of the contact patch from the strain curve, or its derivatives, Figs. 11 and 13 show the extrema of the first derivative of the strain fall well within the patch edges. It follows methods for the footprint detection, under dynamic conditions, based on the distance between these two points [13,14] underestimate the length of the footprint. The second derivative of the tire strain seems a better candidate for the task, in Fig. 14, which has two extrema at the border of the contact patch. The previous observation marks an important and conceptual difference with other techniques, suggesting the points of the tire at the edges of the contact patch that have the highest deformation acceleration in respect to the highest deformation speed [14].

The previous findings will be discussed in detail and are experimentally validated in the next section.

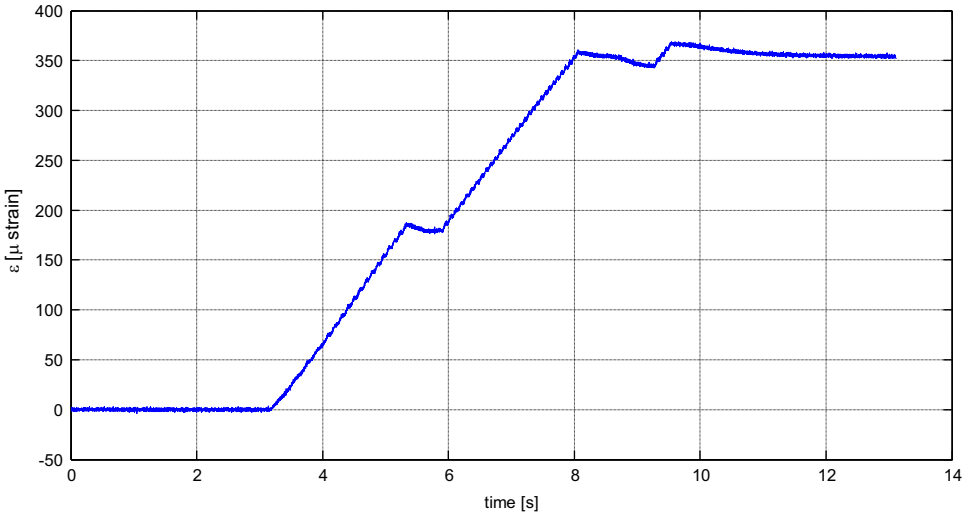

Fig. 15. Tire strain during inflation.

4. Experiments

Fig. 16. Static measurements of the tire footprint.

Some of the acquisition of the test campaign conducted with the experimental setup described in Section 2 is examined in this section. In particular, the strain signals presented here were acquired from one FBG sensor pasted inside the central groove of the tire, along the external circumference, as in Fig. 3. The sampling rate was at least 2.5 kHz and, unless differently specified, the signals were acquired with the intelligent tire mounted on the rear-driving axle.

4.1. Static tests

The first test concerns the acquisition of the circumferential tire deformation during its inflation from 1.7 to 2.3 bar. Fig. 15 shows the time history of the recorded strain signal, where the value at 1.7 bar was used as reference. The deformation linearly grows as the tire is inflated, after 5.5 and 8 s the inflation process was stopped to read the tire pressure gauge. This operation caused air leakage from the tire pressure valve: a small drop of the deformation is indeed observed.

Fig. 16 shows the measurement of the static footprint. The bottom part of the tire was painted with ink and then pressed against a sheet of paper, which lied on the ground. The found dimensions are as follows:

$L = 63$ mm (semifootprint)

$W = 215$ mm (width)

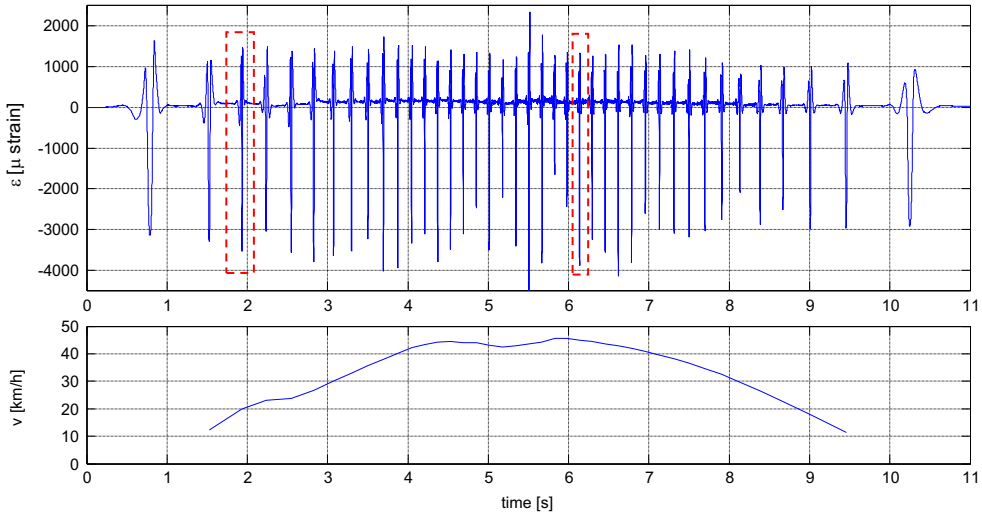

Fig. 17. Starting from the subplot on top, the dynamic strain and the estimated tire velocity plotted versus time.

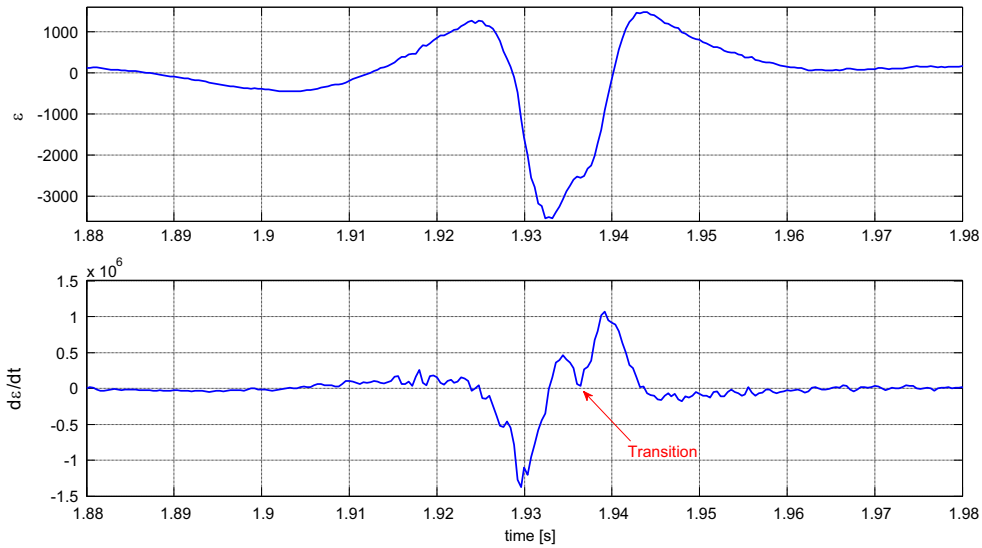

Fig. 18. Magnification of the strain plot in Fig. 17 around 1.93 s, when a strong driving torque is applied. From the subplot on top, the dynamic strain and its first time derivative, plotted versus time.

4.2. Dynamic strain

The second test concerns with the acquisition of the tire strain under dynamic conditions. Fig. 17 shows a typical strain signal with the car undergoing a standing start, an acceleration, a brief uniform speed drive followed by a progressive braking.

The second subplot shows the tire velocity estimated from the strain signal. As outlined in Section 3, the minimum strain points are recorded when the FBG sensor is roughly in correspondence with the centre of the footprint. Given the spatial distance between two consecutive peaks, which is roughly $2\pi R$, the tire speed is numerically estimated with a 2nd order centered differencing formula, with the aid of a peak identification algorithm, i.e. findpeaks function in Matlab^{TM}, applied to the strain time history in Fig. 17.

4.2.1. Experimental evidence of the transition abscissa

Figs. 18 and 19 show the magnification of the strain signal in Fig. 17, when the FBG sensor crosses the contact patch around 1.93 s during hard acceleration, and 6.14 s during gentle braking. Results are in line with the findings of the theoretical model outlined in the previous section:

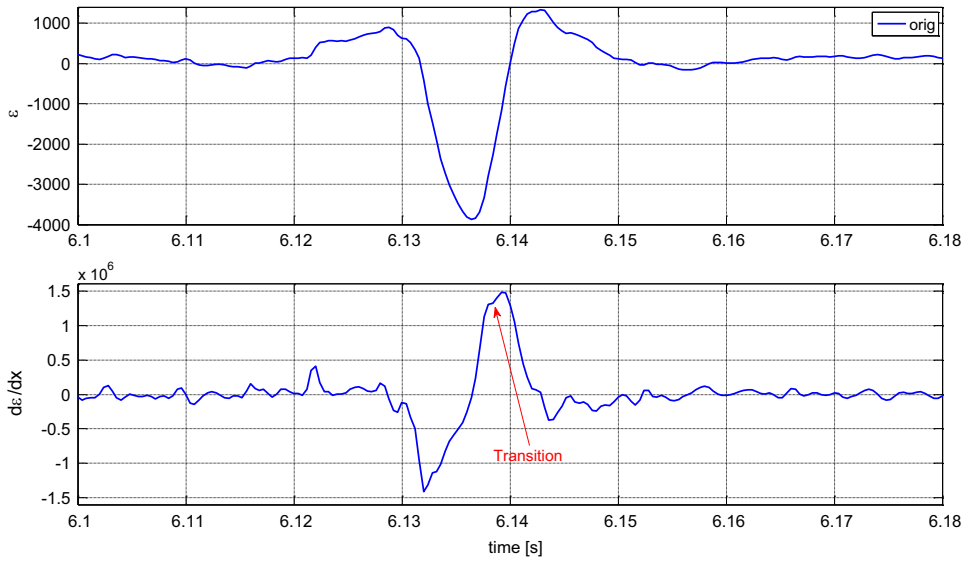

Fig. 19. Magnification of the strain plot in Fig. 17 around 6.14 s, when a gentle braking torque is applied. From the subplot on top, the dynamic strain and its first time derivative, plotted versus time.

a) Recalling that the sensor is placed inside the tire groove, as in Fig. 3, on the outer surface of the tire, the distance from the neutral axis is negative, i.e. $y=-0.1 \bullet h_t/2$, and Eq. (11) confirms the area within the contact patch is mainly compressed.
b) During the first phase of the test the car is accelerating, an intense driving torque is applied to the tire, which causes the sharp rise of the tire velocity in Fig. 17 (the average acceleration is 0.35 g) and makes the slip ratio considerably smaller than zero. As a result the transition abscissa, from the adhesion to the slipping region is clearly identifiable in Fig. 18 at 1935 s, where the strain plot undergoes a sudden slope variation and its derivative has an abrupt change.
c) During the second phase of the test, the driver lifts off the throttle, around $t=6$ s, and pushes progressively the braking pedal. Fig. 19 shows the tire strain during the beginning of the braking phase: the applied torque is modest because the braking circuit takes a brief time interval to be fully effective. Therefore, the slip ratio is small and the transition abscissa is close to the trailing edge, being more difficult to identify from the experimental data. However, a slope variation is still perceptible in the derivative plot, in the neighborhood of 6138 s, which is likely to be located the transition abscissa.

4.3. Dynamic footprint detection

In Section 3 was pointed out that the first derivative of the tire strain has a sharp slope change at the leading and trailing edges, thus the second derivative of the tire strain has two extrema at the border of the contact patch. These theoretical results provide hints to the experimental identification of the tire footprint under dynamic conditions.

On this ground, the technical literature acknowledges several methods; among them the one proposed by Morinaga et al. [14] is one of the most adopted. The technique is based on the assumption that the points with the highest deformation speed are at the edges of the contact patch, thus the distance between the two extrema of the time derivative of the strain is the footprint length. However, theoretical results in Section 3 have shown that the technique underestimates the tire footprint, as in Fig. 11 where the two extrema fall well within the contact patch, and experimental results provided ahead corroborate this idea. As an example, the second subplot in Fig. 19 shows that the extrema are localized at 6.132 and 6.139 s, being the tire velocity 45 km/h and the estimated length of the contact patch [14] 8.7 cm, which is much smaller than the static footprint evaluated in 4.1, roughly 12.6 cm.

As further investigated, Fig. 20 shows a new acquisition where, after a standing start and acceleration, the clutch is put in neutral and the car coasts for the last part of its run. A magnification of Fig. 20 is shown in Fig. 21, which shows the tire strain and its first and second derivatives when the FBG sensors cross the contact patch and the car is coasting. To ameliorate the noise arising from numerical derivatives, a low pass filter is applied to the strain signal. The cut-off frequency is 400 Hz, i.e. roughly 40 times the wheel frequency, and was selected analyzing the spectrum of the first 2 s of the time history of the strain in Fig. 20, acquired with the car at rest.

While the filtered strain signal (in red line) is barely distinguishable from the original one (in blue line), the derivatives of the filtered signal are much smoother.

Fig. 21 shows that the second derivative has two extrema at 18.182 s and 18.214 s, in correspondence the first derivative has sharp slope changes. Being the tire velocity 13.5 km/h, the estimated dynamic length of the contact patch is roughly 12 cm, which seems in line with the measured static length. In comparison, the extrema of the first derivative are localized at 18.185 s and 18.21 s, thus the tire footprint estimation using [14] is much smaller, being 9.3 cm.

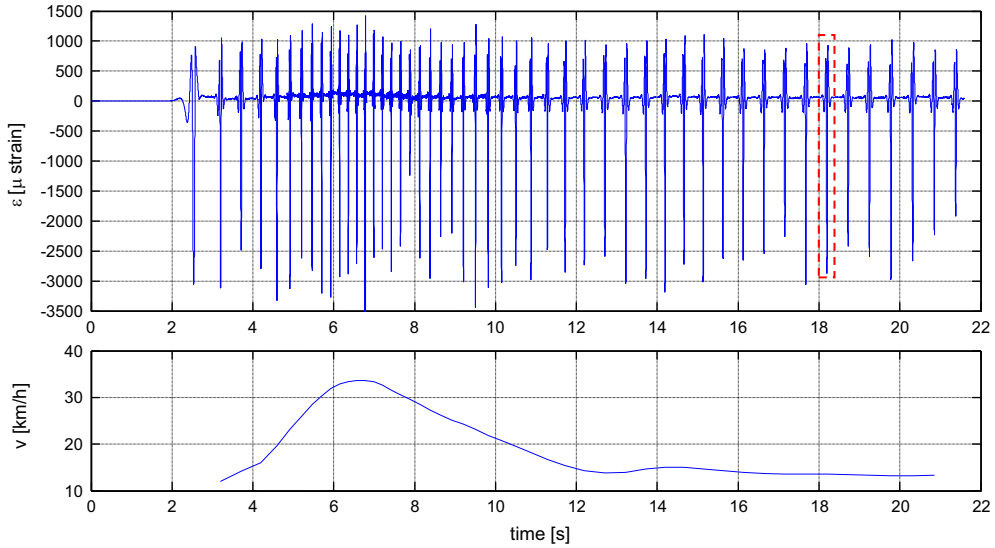

Fig. 20. Starting from the subplot on top, the dynamic strain and the estimated tire velocity plotted versus time. (For interpretation of the references to color in this figure, the reader is referred to the web version of this article.)

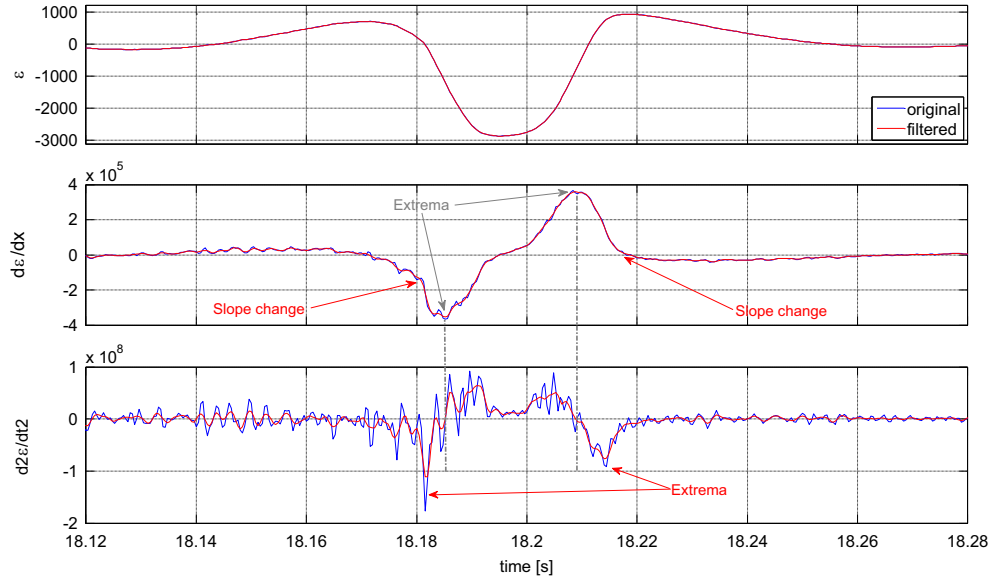

Fig. 21. Magnification of the strain plot in Fig. 20, and its first and second time derivatives, around 18.2 s, blue and red lines are for the original and the filtered (300 Hz low pass frequency) signals, respectively. (For interpretation of the references to color in this figure legend, the reader is referred to the web version of this article.)

The extrema of the second derivative are easy detectable for the remaining part of the signal, as Fig. 22 shows, allowing an easy identification of the tire footprint.

5. Conclusion and perspectives

The experimental and theoretical methodologies presented in this paper set the basis for a new system for the real-time identification of the tire stress during rolling and the residual grip estimation. The original points presented in the previous sections can be summarized as follows:

I. An innovative experimental system based on optical sensor technology is developed and tested with an extensive experimental campaign. The acquired strain signals show the great potential of the present apparatus in respect to the existing technologies: it provides signals with high resolution and accuracy; it does not need complex power supply or data transmission systems, and it is capable of long-term acquisitions, under adverse conditions.

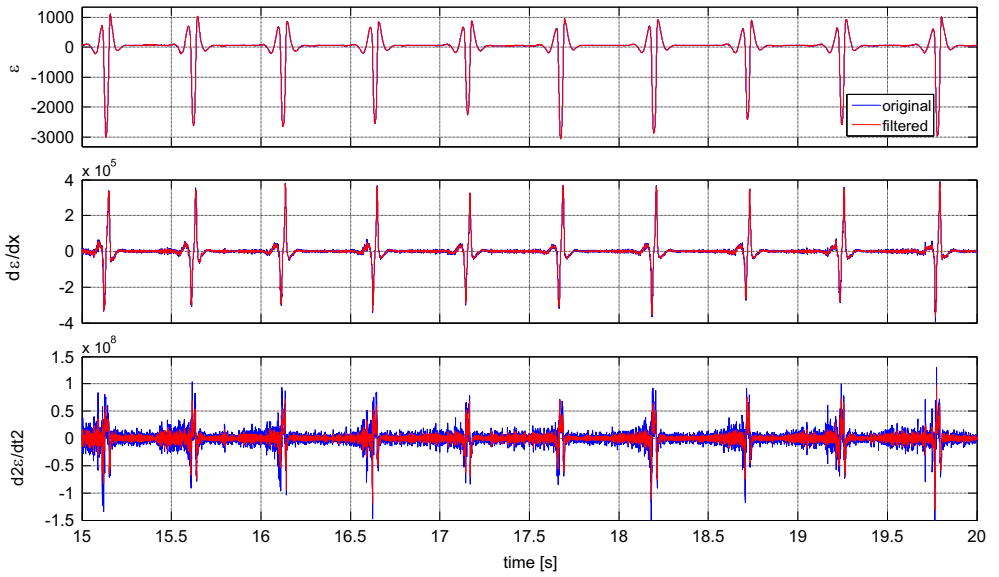

Fig. 22. Magnification of the strain plot in Fig. 20, and its first and second time derivatives, with the time window between 15 and 20 s; blue and red lines are for the original and the filtered, respectively. (For interpretation of the references to color in this figure legend, the reader is referred to the web version of this article.)

II. A new analytical model of the tire is introduced, which helps in interpreting the experimental measurements, based on an infinite beam on elastic foundation able to provide a qualitative yet significant description of the tire–road interaction.
III. Theoretical and experimental results open the way for the real time identification of the tire footprint and of the tire–road grip conditions.

Concerning point (III) results presented in Section 4 show that the real time identification of the length of the contact patch seems to be easier than the one of the residual grip of the tire. In fact, the developed technique suggests the second derivative of the tire strain has two extrema that fall at the border of the contact patch. Using strain signals acquired under dynamic conditions, distances between these points are calculated and result is in line with the measured static footprint of the tire. On this ground it is shown that existing techniques [13,14], which use the distance between the two extrema of the first time derivative of the strain, underestimates the footprint length. This marks a conceptual difference, suggesting the tire segments at the edges of the contact patch have the highest deformation acceleration in respect to the highest deformation speed.

The experimental identification of the tire–road grip condition is strictly related to the position of the transition abscissa along the contact patch. The transition abscissa is clearly identifiable only when an intense torque is applied to the tire, which makes the modulus of the slip ratio considerably greater than zero. For small torques the slip ratio is small and the transition abscissa is close to the trailing edge: under these circumstances the identification becomes more difficult and the process is hindered by ambient and numerical noise together with the needs for high time sampling.

At the moment, a phonic wheel is mounted on the rim and another experimental camping is being carried out to validate the outlined footprint estimation procedure and to get insights into the identification of tire–road grip condition and into rolling resistance and dissipation of the tire.

Finally, the future perspectives of the tire modeling in the context of embedded sensor-based real-time identification techniques deserve a particular mention. In fact, in this paper it has been emphasized how the dedicated models are welcomed. In particular, for real-time sensing, semi-analytical models are particularly appealing, since they permit a higher speed in the real-time data analysis and in the identification process. Under this point of view, the developed analytical model represents a good compromise between a reasonable realistic description of the strain-grip correlation and the need of a sufficiently fast algorithm for real-time use. However, the experience of the Optyre Project has suggested further direction of investigation, also trying to include the following aspects into a relatively simple model: (i) impact dynamics at the leading edge, in a way similar to that presented in [18], (ii) a richer phenomenology in contact mechanics between rough surfaces, making use of the theory in [19], (iii) implementation of new higher-order stress-strain constitutive relationship to account in a synthetic manner of the complex composite structure of the tire, through models close to those in [20], (iv) modeling the contact mechanics in the presence of an interstitial fluid (tire–water–road contact), following some of the ideas contained in [21].

References

[1] L. Chankyu, et al., IEEE/ASME Trans. Mechatron. 9 (2004) 454.
[2] J. Yi, et al., IEEE Trans. Control Syst. Technol. 10 (2002) 381.
[3] Z. Xiangwen et al., IEEE Intelligent Vehicles Symposium Proceedings, 2005, pp. 875–881.
[4] F. Gustafsson et al., SAE Tech. Papers 2001-01-0796, 2001.
[5] M. Nabipoor, et al., J. Phys.: Conf. Ser. 34 (2006) 770.
[6] W. Tjiu et al., IEEE International Conference on Semiconductor Electronics, ICSE 2004, 2004, p. 4.
[7] Jingang Yi, IEEE/ASME Trans. Mechatron. 13 (2008) 95.
[8] A. Pohl, et al., IEEE Trans. Instrum. Meas. 48 (1999) 1041.
[9] S.C. Ergen, A. Sangiovanni-Vincentelli, X. Sun, R. Tebano, S. Alalusi, G. Audisio, M. Sabatini, The tire as an intelligent sensor, computer-aided design of integrated circuits and systems, IEEE Trans. 28 (7) (2009) 941–955.
[10] G. Audisio, The birth of the cyber tyre, solid-state circuits magazine, IEEE Trans. 2 (4) (2010) 16–21.
[11] A. Carcaterra, N. Roveri, Tire grip identification based on strain information: theory and simulations, Mech. Syst. Signal Process. 41 (1–2) (2013) 564–580.
[12] A. Carcaterra, N. Roveri, M. Platini, Device and method for optically measuring the grip of a tyre and tyre suitable for said measuring property, University of Rome “La Sapienza”, first deposit number RM2011A000401, date 27/07/2011.
[13] R. Matsuzaki, N. Hiraoka, A. Todoroki, Y. Mizutani, Analysis of applied load estimation using strain for intelligent tires, J. Solid Mech. Mater. Eng. 4 (10) (2010) 1496–1510.
[14] Morinaga, H., Wakao, Y., Hanatsuka, Y., and Kobayashi, A., The Possibility of Intelligent Tire, in: Proceedings of the 31st FISITA Automotive, Congress. Yokohama, Japan, 2006. p.F2006V104.
[15] A. Doria, L. Taraborrelli and M. Urbani, A modal approach for the study of the transient behavior of motorcycle and scooter tires, in: Proceedings of the ASME 2014 International Design Engineering Technical Conferences and Computers and Information in Engineering Conference, 3, 2014, doi: 10.1115/DETC2014-34023.
[16] B. Glisic, D. Inaudi, Fibre Optic Methods for Structural Health Monitoring, Wiley, New York, 2007.
[17] Y.T. Wei, L Nasdala, H Rothert, Analysis of forced transient response for rotating tires using REF models, J. Sound and Vib. 320 (2009) 145–162.
[18] U. Andreaus, L. Placidi, G. Rega, Soft impact dynamics of a cantilever beam: equivalent SDOF model versus infinite-dimensional system, Proc. Inst. Mech. Eng. C: J. Mech. Eng. Sci. 225 (10) (2011) 2444–2456.
[19] A. Misra, S. Huang, Micromechanics based stress–displacement relationships of rough contacts: numerical implementation under combined normal and shear loading, Comput. Model. Eng. Sci. 52 (2) (2009) 197–215.
[20] F. dell'Isola, P. Seppecher, The relationship between edge contact forces, double forces and interstitial working allowed by the principle of virtual power, C. R. l'Acad. Sci. – Ser. IIb: Mec. Phys. Chim. Astron. 321 (1995) 303–308.
[21] F. dell'Isola, A. Madeo, P. Seppecher, Boundary conditions at fluid-permeable interfaces in porous media: a variational approach, Int. J. Solids Struct. 46 (17) (2009) 3150–3164.
[22] ⟨http://www.smartfibres.com/FBG-interrogators⟩.